Generation of elliptical airy vortex beams based on all-dielectric metasurface

Xiao-Ju Xue(薛晓菊)[1], Bi-Jun Xu(徐弼军)[1,3,†], Bai-Rui Wu(吴白瑞)[1], Xiao-Gang Wang(汪小刚)[1], Xin-Ning Yu(俞昕宁)[1], Lu Lin(林露)[1], and Hong-Qiang Li(李宏强)[2,3]

[1] *School of Science, Zhejiang University of Science and Technology, Hangzhou* 310023, *China*
[2] *Tongji University, Shanghai* 200092, *China*
[3] *Institute of Dongguan-Tongji University, Dongguan* 523808, *China*

(Received 1 April 2022; revised manuscript received 2 June 2022; accepted manuscript online 29 June 2022)

Elliptical airy vortex beams (EAVBs) can spontaneously form easily identifiable topological charge focal spots. They are used for topological charge detection of vortex beams because they have the abruptly autofocusing properties of circular airy vortex beams and exhibit unique propagation characteristics. We study the use of the dynamic phase and Pancharatnam–Berry phase principles for generation and modulation of EAVBs by designing complex-amplitude metasurface and phase-only metasurface, at an operating wavelength of 1500 nm. It is found that the focusing pattern of EAVBs in the autofocusing plane splits into $|m|+1$ tilted bright spots from the original ring, and the tilted direction is related to the sign of the topological charge number m. Due to the advantages of ultra-thin, ultra-light, and small size of the metasurface, our designed metasurface device has potential applications in improving the channel capacity based on orbital angular momentum communication, information coding, and particle capture compared to spatial light modulation systems that generate EAVBs.

Keywords: elliptical airy vortex beams (EAVBs), metasurface, topological charge

PACS: 42.70.–a, 78.67.Pt, 78.67.–n, 78.68.+m **DOI:** 10.1088/1674-1056/ac7cd0

1. Introduction

In 1979, Berry and Balazs first theoretically proposed a special solution to the one-dimensional form of the Schrödinger equation, i.e., the airy wave packet.[1] In 2007, Siviloglou *et al.* introduced finite energy airy beams by theoretical derivation and experimental demonstration.[2] Airy beams can exhibit intriguing properties, such as diffraction-free propagation, self-acceleration, and self-healing. In recent few years, airy beams have been extensively investigated theoretically for their outstanding properties, including the study of two-dimensional airy beams.[3–6] Subsequently, the circularly symmetric form of airy beams was first proposed by Efremidis and Christodoulides in 2010.[7] This symmetric airy beam exhibits abruptly autofocusing properties, that is, the energy of the beam is small in the propagation process, while the maximum light intensity at the focusing point increases rapidly to achieve abrupt focusing.[8] The interesting behavior exhibited by circular airy beams has great applications in many fields such as optical bullets,[9] biomedical processing, and atomic manipulation.[8,10] In recent years, the polarization conversion and propagation characteristics of different forms of circular airy beams in media have been studied.[11,12]

The vortex beam, which is a special beam with spiral structure in the isotropic plane and carries orbital angular momentum,[13] was first proposed by Coullet *et al.* in 1989.[14] So far, many types of vortex beams have been proposed around the unique properties of vortex beams, which have also found significant applications in optical communication,[15–17] particle rotation, and detection.[18–20] The combination of vortex beams and airy beams also has great potential applications, such as airy vortex beams and circular airy vortex beams. Researchers have been investigated the orbital angular momentum and spin angular momentum conversion relationship of light near the autofocusing plane,[21] particle trapping and improving the interference immunity of optical communication.[22–25] In 2018, Zha *et al.*[26] extended circular airy beams to elliptical airy beams and discovered the unique properties of elliptical airy beams from theoretical and experimental aspects. In that year, Xie *et al.*[27] proposed elliptical airy beams with and without vortex phase, and investigated the interesting phenomena in the propagation process based on the asymmetry of elliptical airy beams. In 2020, Cao *et al.*[28] studied the propagation characteristics of EAVBs under circular concentric vortex, including the characteristics of EAVBs on the autofocusing plane, and generated EAVBs through experiment. They found that EAVBs can produce spots with one more bright spots in the focal plane than the topological charge, and the bright spots at the ends have higher energy. Based on the significant characteristics of this special beam, it can be used for particle capture,[22] topological charge (TC) detection,[19,29] and optical micro-manipulation.[30]

Metasurfaces are two-dimensional thin planar devices composed of arrays of subwavelength resonant units,[31–36] which are an extension and expansion of metamaterials re-

†Corresponding author. E-mail: xubijun@zust.edu.cn

© 2023 Chinese Physical Society and IOP Publishing Ltd

search. By combining resonant units with different structural parameters in a specific way, dynamic modulation of electromagnetic wave amplitude, phase, and polarization mode can be achieved. In order to avoid the ohmic loss induced by metallic materials and to improve the beam transmission efficiency at high frequency bands, researchers tend to choose dielectric nanomaterials with larger refractive index to constitute all-dielectric metasurface,[37–39] so as to achieve smaller loss, higher diffraction, and transmission efficiency. In addition, many planar optical elements can be realized by using metasurfaces, such as planar lens,[40–42] special beams,[43–45] and holographic imaging.[46–48] However, the problem is that most of the metasurface devices that achieve beam modulation only measure the phase parameter of the incident light and achieving efficient metasurfaces that control both amplitude and phase is still a source of motivation to keep moving forward in the quest. Recently, complex-amplitude metasurfaces have been used in the field of holographic imaging. The demonstrations of complete complex-amplitude holograms with subwavelength definition at visible wavelengths are achieved and show excellent performances with remarkable signal-to-noise ratio compared to traditional phase-only holograms.[49–51] In addition, as far as we know, no one has used the metasurface technology to generate EAVBs.

In this paper, we propose a new method of all-dielectric metasurface for generating EAVBs in the near-infrared region. Combining the principles of geometric phase and waveguide phase modulation, the polarization conversion rate and transmittance of the transmitted optical field are varied by controlling the geometry and rotation angle of the nanopillar under the vertical incidence of lefthanded (LCP) or right-handed (RCP) circularly polarized light. Based on the different modes of modulation of the incident light degrees of freedom, we design complex-amplitude and phase-only metasurfaces, respectively. The results show that both of our designed metasurfaces can generate the expected EAVBs. Changing the topological charge causes the focus pattern of the EAVBs to change and its autofocusing position to remain essentially unchanged. Finally, we compare the subtle differences between the two metasurfaces, namely, in terms of the focus position of the generated beam and the depth of focus obtained from the achieved results. Compared the spatial light modulator with the $4f$ system, our designed metasurface device is simple, lightweight, and miniaturized, which provided a novel idea for realizing EAVBs and expected to replace the equipment-intensive beam generators.

2. Theory and design

We build a meta-atom library using the degree of birefringence and rotation angle of the single nanopillar meta-atom for achieving combined amplitude and phase modulation. The rectangular silicon nanopillar acts as a birefringent medium with different amplitudes and phase responses for the components polarized along its normal and special axes, respectively. If the amplitude is completely controlled by the degree of birefringence of the meta-atom shape, the maximum optical amplitude can be generated. According to Ref. [52], when the incident light is left-handed circularly polarized light or right-handed circularly polarized light, amplitude can also be considered as the conversion amplitude when transmission amplitudes $T_o = T_e$ along the ordinary and extraordinary axes of meta-atom, that is,

$$\eta_{\text{conversion}} = \sin\left(\frac{k_0 d\,(n_o - n_e)}{2}\right), \tag{1}$$

where $k_0 = 2\pi/\lambda_0$, $\lambda_0 = 1.55$ μm, d is height of meta-atom, n_o and n_e are refractive indexes along the ordinary and extraordinary axes of meta-atom. Figure 1(a) presents a schematic diagram of all-dielectric metasurface for generating EAVB. Here, we choose the lattice constant $P = 0.7$ μm and nanopillar height $H = 0.8$ μm. The geometric parameters of the meta-atom are scanned by the time-domain finite-difference solver, and the length of the optimized rectangular nanopillar length is set to $W_x = 0.24$ μm, which almost satisfies $T_o = T_e = 1$. According to the geometric phase principle, the right-handed component of the transmitted light (T_{RCP}) is the reversed part when the incident light is LCP. The left-handed component (T_{LCP}) cannot be utilized in the transmitted light. Therefore, we define the figure of merit FOM $= T_{\text{RCP}} - T_{\text{LCP}}$ to describe the ability of the meta-atom to convert the polarization state of the light. As shown in Fig. 1(b), the spatial geometry of the nanopillar meta-atom is continuously changed to ensure efficient transmission efficiency and to achieve perfect conversion of the polarization state. When the conversion efficiency of the nanopillar varies from 0 to 1 corresponding to the change in width W_y from 0.34 μm to 0.43 μm taking values, the transmitted light through the nanopillar meta-atom exhibits high transmittance. In the present work, the simulation is performed by using the finite difference method in the time domain (FDTD solutions, Lumerical Inc.) in Lumerical software. Periodic boundary conditions are used in the x and y directions, and perfectly matched layer (PML) boundary conditions are used for the z boundary. The polarization state of the incident light is LCP light in the simulation. After determining the range of values of W_x and W_y, according to the geometric phase principle, we introduce the rotation angle α, that is, the phase change is doubled with the rotation angle of the unit cell. When W_y changes from 0.34 μm to 0.46 μm, and the meta-atom rotation angle α changes from 0° to 180°, the meta-atom amplitude changes from 0 to 1, and the phase delay of the transmitted light is sufficient to cover the whole 2π region, as shown in Figs. 1(c)–1(f). After designing the single nanopillar meta-atom, the initial optical field of the EAVB is then reproduced and the built-up unit cells are arranged into

metasurface structure. The initial plane electric field distribution of the EAVB is defined as[28]

$$U_{\text{evab}} = \text{Ai}\left(\frac{r_0-\sqrt{x^2+t^2y^2}}{w}\right) \times \exp\left(a\frac{r_0-\sqrt{x^2+t^2y^2}}{w}\right)\exp(im\theta). \quad (2)$$

Here Ai is the airy function, $w = 2$ represents the scale factor of the elliptical airy beam, $r_0 = 15$ μm is a parameter related to the size of the main ring in the initial plane of the elliptical airy beam, m represents the topological charge of the point vortex, $\theta = \arctan(y/x)$ represents the angular coordinates of the field point (x, y), and is specified as $0 < t < 1$. In our design, we set $t = 0.7$, $x = [-49\,\mu\text{m}, 49\,\mu\text{m}]$, $y = [-49\,\mu\text{m}, 49\,\mu\text{m}]$.

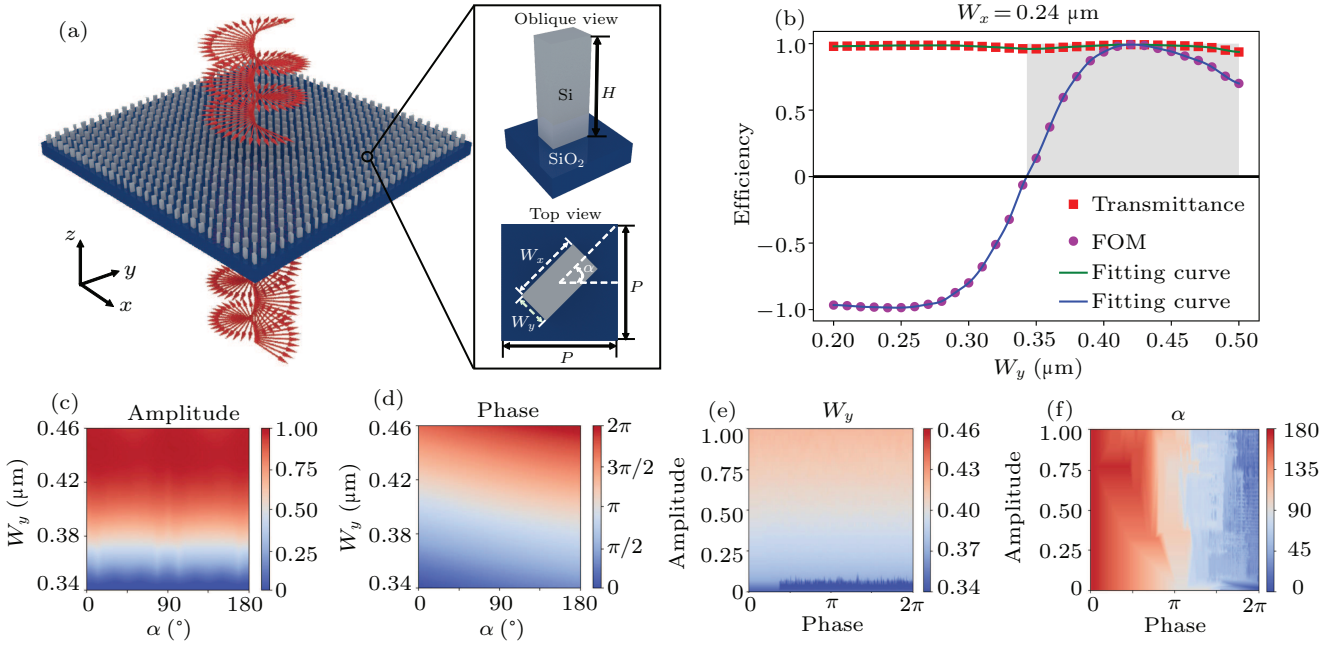


Fig. 1. (a) Schematic generation of EAVBs propagation after vertical incidence of the LCP onto complex-amplitude metasurface. After amplifying the metasurface array, oblique and top views of single nanopillar meta-atom are displayed. (b) When $W_x = 0.24$ μm, W_y changes from 0.2 μm to 0.5 μm, the transmittance of meta-atom remains to be around 1. The polarization conversion efficiency varies dynamically and continuously between −1 and 1, indicating that the incident light for circular polarized light can be achieved. The red squares and purple circles are the transmittance and polarization conversion efficiency sampling points scanned during the simulation, respectively, and the green and blue solid lines are the corresponding fitting curves. We cover the part of the scattering efficiency and polarization conversion efficiency greater than zero with gray area. (c) and (d) The variation of the amplitude and phase of the transmitted light field with the width and rotation angle of the silicon nanopillar, simulated by scanning the parameters. (e) and (f) W_y and α look-up charts generated by processing the data obtained from (c) and (d), from which we can find the W_y and α values corresponding to arbitrary amplitudes and phases.

3. Results and analysis

3.1. Phase-only metasurface

Based on the geometric phase modulation method, we choose the optimal nanopillar length-to-width ratio under the condition of constant height, and design the phase-only metasurface to generate EAVBs according to the different rotation angles of the nanopillars at different positions. The specific parameters of the nanopillar are set to $W_x = 0.24$ μm and $W_y = 0.42$ μm. Figures 2(a) and 2(b) show the light intensity and phase distribution of the initial light field of the EAVB generated according to Eq. (2). Figures 2(c) and 2(d) show the x–y plane light intensity distribution and phase distribution generated by the phase-only metasurface in the near-field region, and the simulation data are extracted from the monitor at the distance of half the working wavelength from the metasurface. We can find that even if each nanopillar only modulates the phase of the light field, the light intensity part shown in the figure still conforms to the light intensity distribution of the EAVB. By comparing several figures, it can be seen that the phase-only metasurface realization of our design is similar to the theoretical simulation results. The simulation results show that the overall transmission efficiency of the designed phase-only metasurface is approximately 35%. Note that the phase distribution actually satisfies $\phi = \varphi_{\text{evab}} + \varphi_0$ in the actual design of the metasurface. Here $\varphi_{\text{evab}} = \text{angle}(U_{\text{evab}})$, and φ_0 is a randomly chosen reference phase. Since phase-only metasurface is less complex to design than complex-amplitude metasurface, many design errors can be avoided and the final result is better than that of complex-amplitude metasurface. When $t = 1$ and $m = 1$, the beam produced by the metasurface is a circular airy vortex beam with topological charge of 1. The circular symmetric airy beam has a self-focusing property, and the light intensity distribution shows a kind of hollow ring pattern at the focusing position because it carries the vortex angular momentum propagation trajectory of the circularly symmetric airy vortex beam produced by a phase-only metasurface.

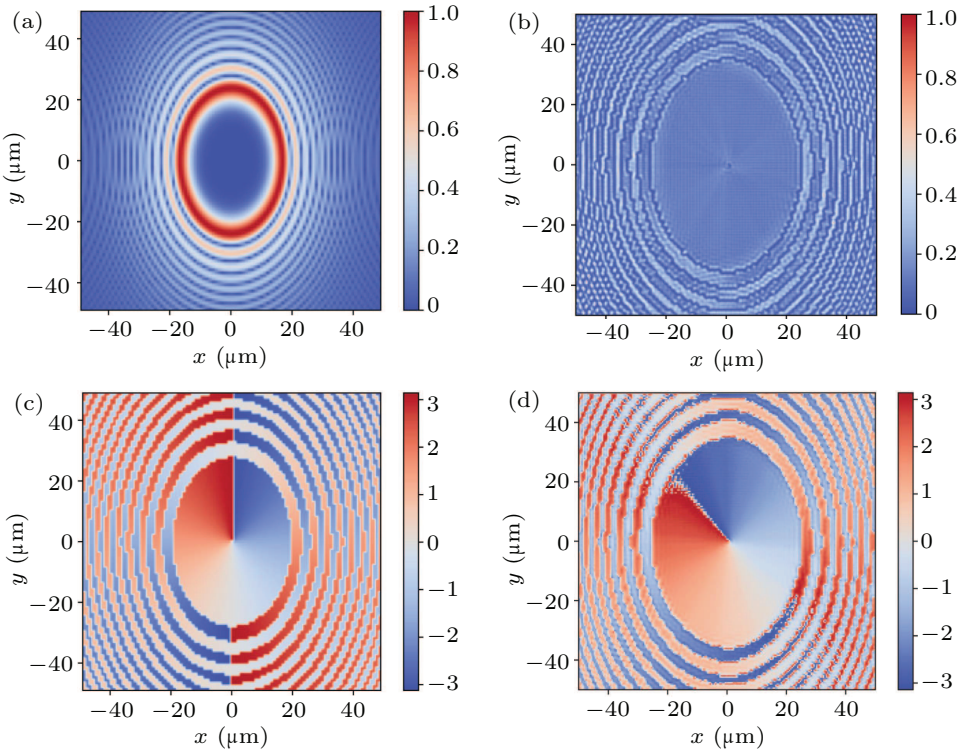


Fig. 2. Simulation of the initial planar EAVB produced by phase-only metasurface in the near-field region. (a) and (b) The initial light intensity and phase distribution in the *x*–*y* plane obtained from the simulation of the theoretical equation. (c) and (d) The simulation results of the *x*–*y* plane light intensity and phase distribution extracted along the beam propagation direction, that is, at one-half wavelength position from the metasurface.

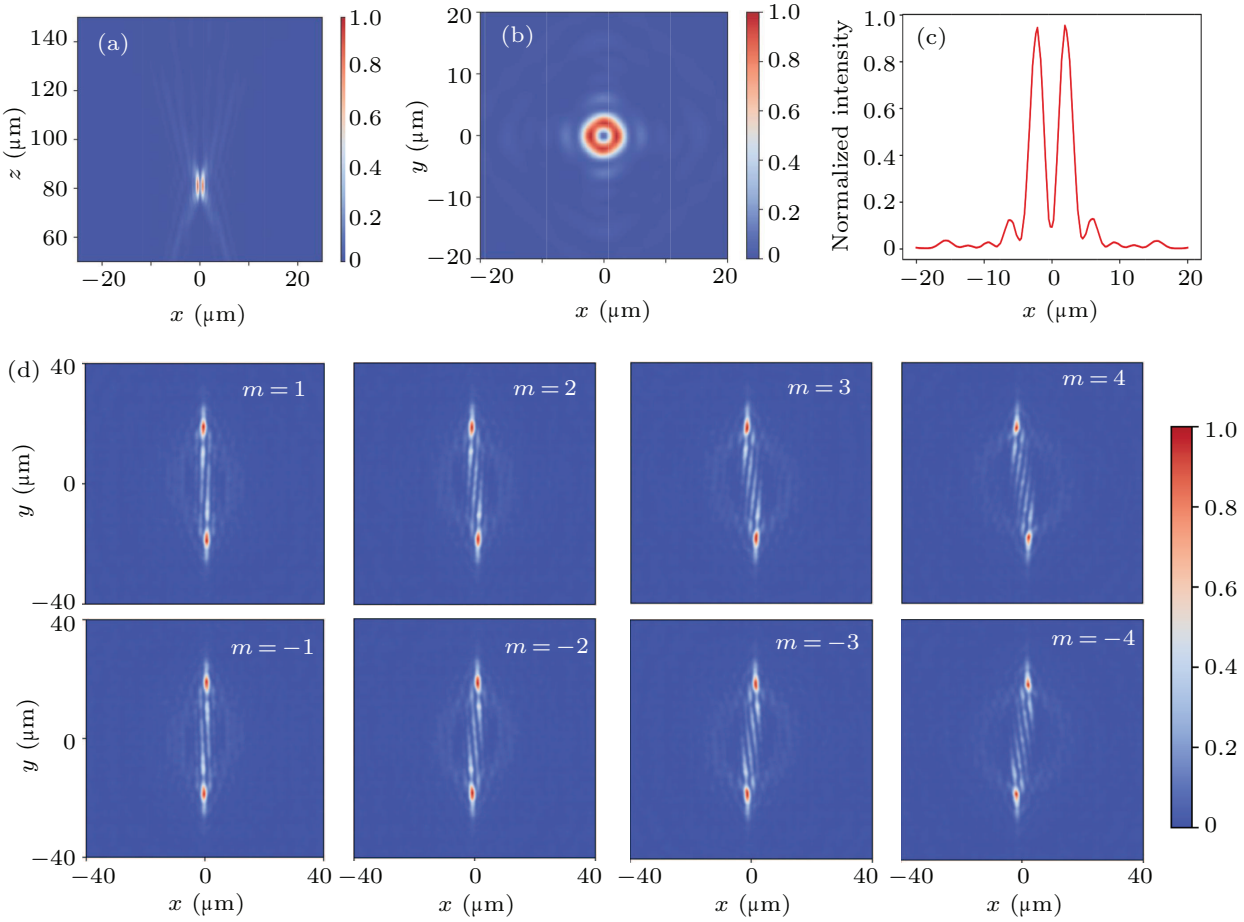


Fig. 3. (a) The propagation characteristics of circularly symmetric airy vortex beam generated by phase-only metasurface. (b) Contour diagram of the light intensity at the focal position. (c) The relationship between light intensity and position at the focal position. (d) Light intensity distribution at the beam convergence for EAVBs with topological charges of ±1, ±2, ±3, and ±4, respectively.

Figure 3(a) demonstrates the propagation characteristics of circularly symmetric airy vortex beam generated by phase-only metasurface. Figure 3(b) depicts a cross-sectional light intensity field map at the focal position. Figure 3(c) presents the light intensity distribution curve along the x-axis in the focal plane extracted from Fig. 3(b). It can be seen that the light intensity at the center of the focal position is nonzero, which may be caused by a small amount of co-polarized circularly polarized light. From the propagating light field of the circularly symmetric airy vortex beam, the focusing position of the general EAVB can be determined. The theoretical focus position is predicted by the equation $z_f \cong 2kw^2\sqrt{\frac{c}{w}+1.02}$. The focal position of the beam simulation results for phase-only metasurface generation is at $z_{f_1} \cong 84$ μm. The EAVB is more general and complex than the circular symmetric vortex airy beam. When $t \neq 1$, the initial light field spot main ring presents an elliptical shape, that is, the short axis of the main ring is more focused than the long axis. In this study, we set $t = 0.7$, because the initial planar halo pattern of EAVB presents asymmetry, which will produce different transmission characteristics from the circular symmetric airy vortex beam, so the beam propagation trajectory will be different at the beam convergence. We reproduce the EAVBs carrying different topological charge numbers by using metasurface and verify the light field distribution properties at the beam convergence by simulation. Figure 3(d) shows the light intensity distribution at the convergence position for the EAVBs with topological charges of ±1, ±2, ±3, and ±4, respectively. It can be observed that there are two highest energy points along the long axis and two "tails" of relatively high light intensity extending toward the center of the light field. In addition, as the topological charge number increases, two additional long focal points appear in the middle of the two maximum light intensity focal points, and their number is related to the topological charge number as $|m|-1$. The larger the topological charge $|m|$, the further the lateral offset from the central axis, and more 'tails' appear between the two focal points of maximum light intensity. In addition, the focal pattern size becomes larger, and the focus of the EAVB is more tilted from the overall view. The direction of the focal spot tilt is related to the sign of m. When the topological charge number is positive, the focal spot tilts from bottom to top to the left, and when the topological charge number is negative, the focal spot tilts from bottom to top to the left.

3.2. Complex-amplitude metasurface

The complex-amplitude metasurface is a metasurface with simultaneous control of phase and amplitude. The two optical parameters are regulated by combining the transmission phase and geometric phase principles to achieve continuous manipulation of the optical field. The complex-amplitude metasurface is composed of rectangular silicon nanopillars of different sizes and different rotation angles on silicon dioxide substrate. The whole array area of about 98 μm × 98 μm. By reconstructing the light field of EAVB, the transmitted right-handed circularly polarized light forms EAVB in free space. Figure 4 shows all the information on the amplitude and phase of the EAVB extracted from the near-field region. Comparison with the theoretical formula shown in Figs. 2(a) and 2(b) proves that the normalized light intensity distribution profiles are generally the same. Since the interpolation method is used to design and build the library, the phase distribution will have a little deviation at some positions, whereas the distribution is roughly the same. The simulation results show that the overall transmission efficiency of the designed complex-amplitude metasurface reaches approximately 34%.

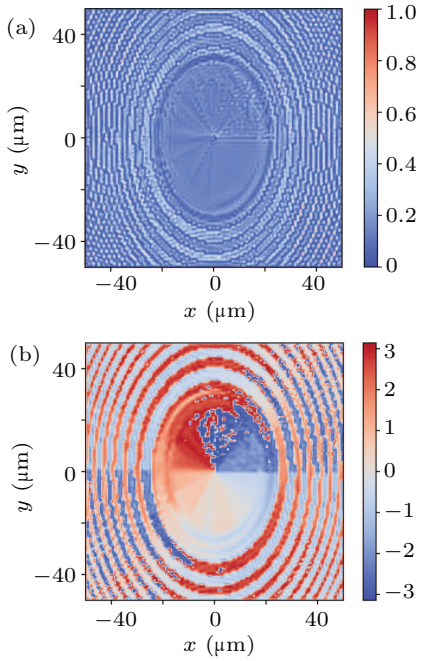


Fig. 4. Simulated transverse planar field profile of EAVBs generated by complex-amplitude metasurface. (a) and (b) The simulation results of the amplitude and phase distribution in the x–y plane extracted at one-half wavelength position along the z-axis from the metasurface.

Figure 5(a) is a schematic diagram of the propagation trajectory of the circularly symmetric airy vortex beam produced by the LCP incident vertically onto the complex-amplitude metasurface at $t = 1$ and $m = 1$. During the simulation, we place the field monitor at about one-half of the wavelength from the metasurface, which is used to record the full intensity and phase information of the optical field. Figure 5(b) is a cross-sectional light intensity field map at the focal position. Figure 5(c) is the light intensity distribution curve along the x-axis in the focal plane extracted from Fig. 5(b). Since the necessary data interpolation methods are used to build the meta-atom diagrams, there are errors in the geometric parameters of a few unit cells in the overall complex-amplitude metasurface, which may also lead to partial deviations in the intensity and phase to be reconstructed, achieving a little weaker performance than the phase-only metasurface.

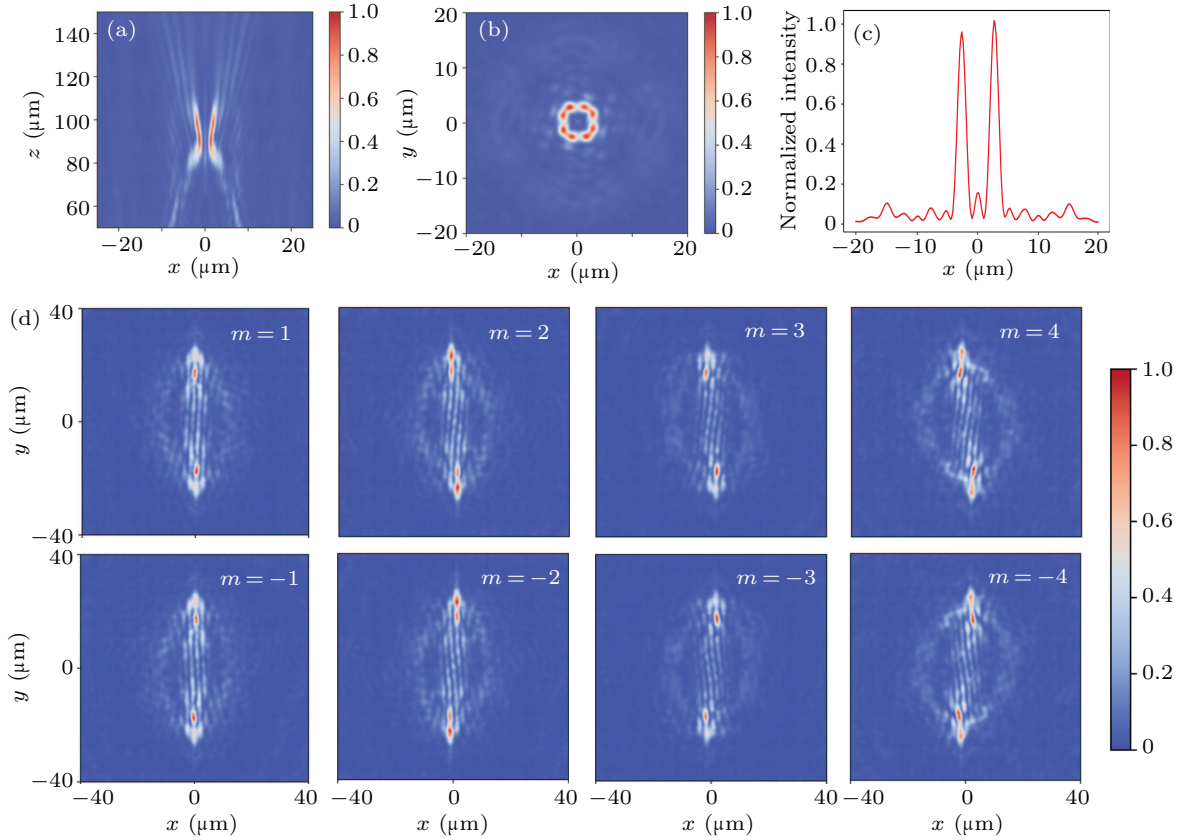


Fig. 5. (a) Propagation of circularly symmetric airy vortex beams generated by complex-amplitude metasurface. (b) Light intensity distribution at the focal position. (c) The relationship between light intensity and position is extracted on the basis of (b). (d) The light intensity distribution at the beam convergence for EAVBs with topological charges of ±1, ±2, ±3, and ±4, respectively.

The focus position of the metasurface is at $z_{f_2} \cong 95$ μm, and the intensity of the profile light field is shown in Fig. 5(d). Due to the design defects, the light intensity distribution on the ring is not very uniform. In addition, there are still some left-handed circular polarized lights in the whole free space, that is, the part of the light that is not reasonably regulated by the metasurface, which has a certain impact on the final results. In practical applications, the polarizer can be used to filter out some of the useless light, thus improving the efficiency of the device. Comparing the two different modulation methods of the metarsurface devices, it can be found that the phase-only metasurface is relatively simple in terms of design complexity and also produces good results. The complex-amplitude metasurface does not perform as well as the phase-only metasurface in the end due to design flaws. However, the complex-amplitude metasurface also has its advantages. First, the focusing position of EAVB generated is closer to the theoretical value (theoretical value $z_f \cong 92$ μm, the focusing position $z_{f_1} \cong 84$ μm of the beam generated by the phase-only metasurface, and the focusing position $z_{f_2} \cong 95$ μm of the beam generated by the complex-amplitude metasurface). Second, the depth of focus of the beam produced by the complex-amplitude metasurface is greater than that of the phase-only metasurface, which can be demonstrated by comparing Fig. 3(a) with Fig. 5(a).

4. Conclusion

In summary, we have numerically demonstrated an EAVB generated in the near-infrared region based on the all-dielectric metasurface. The EAVB has self-focusing properties and spontaneously forms easily identifiable topological charge focal spots, which can be applied in TC capture and detection. We combine the geometric phase and waveguide phase modulation principles to design phase-only and complex-amplitude metasurfaces to generate and modulate EAVBs under the incidence of circularly polarized light by changing the geometric width and rotation angle of the nanopillar, respectively. The results show that both phase-only and complex-amplitude metasurfaces produce the expected elliptical airy vortex spots, and the focusing mode splits into a total of $|m|+1$ bright spots at the focal plane. The long bright spot for topological charge $m > 0$ is tilted to the left while the long bright spot for $m < 0$ is tilted to the right. Such metasurface devices may be used to improve communication quality and information coding, and accurately to adjust the position of captured particles.

Acknowledgements

Project supported by the National Natural Science Foundation of China (Grant No. 61975185), and the Natural Science Foundation of Zhejiang Province, China (Grant Nos. LY19F030004 and LY20F050002).

References

[1] Berry M V and Balazs N L 1979 *Am. J. Phys.* **47** 264
[2] Siviloglou G A, Broky J, Dogariu A and Christodoulides D N 2007 *Phys. Rev. Lett.* **99** 213901
[3] Li Z, Cheng H, Liu Z, Chen S and Tian J 2016 *Adv. Opt. Mater.* **4** 1230
[4] Hao W, Deng M, Chen S and Chen L 2019 *Phys. Rev. Appl.* **11** 054012
[5] Wen J, Chen L, Yu B, Nieder J B, Zhuang S, Zhang D and Lei D 2021 *ACS Nano* **15** 1030
[6] Wu B, Xu B, Wang X and Ying H 2021 *Opt. Mater. Express* **11** 842
[7] Efremidis N K and Christodoulides D N 2010 *Opt. Lett.* **35** 4045
[8] Papazoglou D G, Efremidis N K, Christodoulides D N and Tzortzakis S 2011 *Opt. Lett.* **36** 1842
[9] Panagiotopoulos P, Papazoglou D G, Couairon A and Tzortzakis S 2013 *Nat. Commun.* **4** 2622
[10] Manousidaki M, Papazoglou D G, Farsari M and Tzortzakis S 2016 *Optica* **3** 525
[11] Jiang Y, Yu W, Zhu X and Jiang P 2018 *Opt. Express* **26** 23084
[12] Li T, Cao B, Zhang X, Ma X, Huang K and Lu X 2019 *J. Opt. Soc. Am. A* **36** 526
[13] Marrucci L, Manzo C and Paparo D 2006 *Phys. Rev. Lett.* **96** 163905
[14] Coullet P, Gil L and Rocca F 1989 *Opt. Commun.* **73** 403
[15] Wang J, Yang J Y, Fazal I M, Ahmed N, Yan Y, Huang H, Ren Y, Yue Y, Dolinar S, Tur M and Willner A E 2012 *Nat. Photon.* **6** 488
[16] Kai C, Huang P, Shen F, Zhou H and Guo Z 2017 *IEEE Photon. J.* **9** 7902510
[17] Wang Z, Zhang N and Yuan X C 2011 *Opt. Express* **19** 482
[18] He H, Friese M E J, Heckenberg N R and Rubinsztein-Dunlop H 1995 *Phys. Rev. Lett.* **75** 826
[19] Ding L, Meng Z, Feng S, Nie S, Ma J and Yuan C 2020 *IEEE Photon. Technol. Lett.* **32** 741
[20] Ruelas A, Lopez-Aguayo S and Gutiérrez-Vega J C 2018 *J. Opt.* **21** 015602
[21] Nieminen T A, Stilgoe A B, Heckenberg N R and Rubinsztein-Dunlop H 2008 *J. Opt. A: Pure Appl. Opt.* **10** 115005
[22] Chen M, Mazilu M, Arita Y, Wright E M and Dholakia K 2013 *Opt. Lett.* **38** 4919
[23] Wang X, Yang Z and Zhao S 2019 *Optik* **176** 49
[24] Datta A and Saha A 2020 *Optik* **218** 165006
[25] Yu L and Zhang Y 2017 *Opt. Express* **25** 22565
[26] Zha Y, Huang K, Liu B, Sun M, Hu H, Li N, Zhang X, Zhu B and Lu X 2018 *Appl. Opt.* **57** 6717
[27] Xie W, Zhang P, Wang H and Chu X 2018 *Opt. Commun.* **427** 288
[28] Cao B, Shen D, Qiu Z, Li T, Huang K, Zhang X and Lu X 2020 *J. Opt. Soc. Am. A* **37** 1883
[29] Dwivedi R, Sharma P, Jaiswal V K and Mehrotra R 2021 *Opt. Commun.* **485** 126710
[30] Zhang Y, Zeng X, Ma L, Zhang R, Zhan Z, Chen C, Ren X, He C, Liu C and Cheng C 2019 *Adv. Opt. Mater.* **7** 1900372
[31] Yu N, Genevet P, Kats Mikhail A, Aieta F, Tetienne J P, Capasso F and Gaburro Z 2011 *Science* **334** 333
[32] Chen L, Li H, Hao W, Yin X and Wang J 2020 *Chin. Phys. B* **29** 084210
[33] Lin B Q, Lv L T, Guo J X, Wang Z L, Huang S Q and Wang Y W 2020 *Chin. Phys. B* **29** 104205
[34] Wu J Y, Xu X F and Wei L F 2020 *Chin. Phys. B* **29** 094202
[35] Zhang Z Y, Fan F, Li T F, Ji Y Y and Chang S J 2020 *Chin. Phys. B* **29** 078707
[36] Zhou C and Li J S 2020 *Chin. Phys. B* **29** 078706
[37] Nadell C C, Huang B, Malof J M and Padilla W J 2019 *Opt. Express* **27** 27523
[38] Liu H, Guo C, Vampa G, Zhang J L, Sarmiento T, Xiao M, Bucksbaum P H, Vučković J, Fan S and Reis D A 2018 *Nat. Phys.* **14** 1006
[39] Yang W, Xiao S, Song Q, Liu Y, Wu Y, Wang S, Yu J, Han J and Tsai D P 2020 *Nat. Commun.* **11** 1864
[40] Khorasaninejad M, Aieta F, Kanhaiya P, Kats M A, Genevet P, Rousso D and Capasso F 2015 *Nano Lett.* **15** 5358
[41] Arbabi E, Arbabi A, Kamali S M, Horie Y, Faraji-Dana M and Faraon A 2018 *Nat. Commun.* **9** 812
[42] Wan X, Xiang Jiang W, Feng Ma H and Jun Cui T 2014 *Appl. Phys. Lett.* **104** 151601
[43] Wu B, Xu B, Li Z, Cheng P, Xue X, Sun Z, Wang J, Wang Y, Zhi Y, Lin L, Wang X and Hao Y 2021 *Opt. Mater. Express* **11** 1383
[44] Sun Z C, Yan M Y and Xu B J 2020 *Chin. Phys. B* **29** 104101
[45] Xu B, Wu C, Wei Z, Fan Y and Li H 2016 *Opt. Mater. Express* **6** 3940
[46] Li L, Jun Cui T, Ji W, Liu S, Ding J, Wan X, Bo Li Y, Jiang M, Qiu C W and Zhang S 2017 *Nat. Commun.* **8** 197
[47] Ni X, Kildishev A V and Shalaev V M 2013 *Nat. Commun.* **4** 2807
[48] Wang X, Wang W, Wei H, Xu B and Dai C 2021 *Opt. Lett.* **46** 5794
[49] Deng Z L, Jin M, Ye X, Wang S, Shi T, Deng J, Mao N, Cao Y, Guan B O, Alù A, Li G and Li X 2020 *Adv. Funct. Mater.* **30** 1910610
[50] Jiang Q, Cao L, Huang L, He Z and Jin G 2020 *Nanoscale* **12** 24162
[51] Lee G Y, Yoon G, Lee S Y, Yun H, Cho J, Lee K, Kim H, Rho J and Lee B 2018 *Nanoscale* **10** 4237
[52] Overvig A C, Shrestha S, Malek S C, Lu M, Stein A, Zheng C and Yu N 2019 *Light Sci. Appl.* **8** 92